Electronic Supplementary Information

Title: Local heterojunction of Atomic Pt cluster boosts the oxygen reduction activity of RuCore@PdShell nanocrystallite

Authors: *Jeng Han Wang,[a] Kuan-Wen Wang,[b*] Tian-Lin Chen,[a] Chia-Hsin Wang,[c] Yu-Ming Huang,[d] Yang-Yang Hsu,[d] and Tsan-Yao Chen,[d,e*§]*

Affiliations:

a. Department of Engineering and System Science, National Tsing Hua University, Hsinchu 30013, Taiwan.

b. Institute of Nuclear Engineering and Science, National Tsing Hua University, Hsinchu 30013, Taiwan.

c. Department of Chemistry, National Taiwan Normal University, Taipei 106, Taiwan.

d. Institute of Materials Science and Engineering, National Central University, Taiwan

e. National Synchrotron Radiation Research Center, Hsinchu 30013, Taiwan.

*To whom correspondence should be addressed:

Tsan-Yao Chen, email: chencaeser@gmail.com Tel: +886-3-5715131#34271;

1. The DFT results of model with Pt clusters in different configurations.

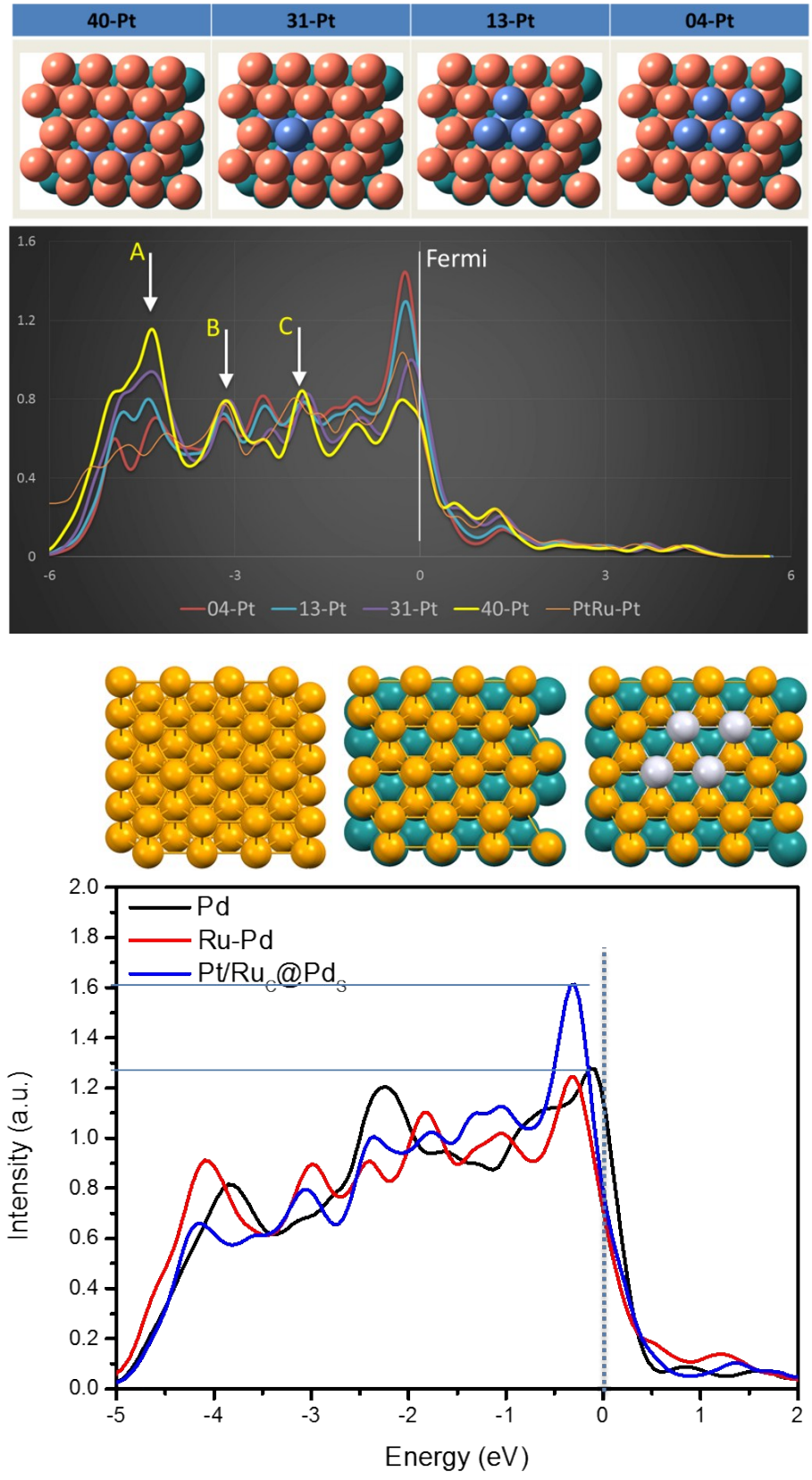

Fig. S1. The DFT calculated DOS of Pd, Ru-Pd, and Pt/Ru$_C$@Pd$_S$ models

As indicated, the DOS in near-Fermi level of $Pt/Ru_C@Pd_S$ is substantially increased by 3.1 (a.u) compared to that of Pd and Ru-Pd NPs. This feature indicates the electronic relocation from substrate to the near-surface region.

2. Photoemission quantitation analysis methods for XPS depth profile

XPS spectra was collected at the Wide Range SGM Beamline (BL24A) of the National Synchrotron Radiation Research center. The WR-SGM beamline is based on the Dragon type design, six-meter SGM with bending magnet source, and delivers photons over a wide spectral range from 10 to 1500 eV. Two movable entrance slits in conjunction with a shared movable exit slit are employed to accommodate the requirement of different grating included angles for low- and high-energy branches. Gas-phase photoabsorption measurements performed on various gases validate that the resolution is at least 20000 in the low-energy branch and 8000 in the high-energy branch. The resolution data compare well with the theoretical calculation. The photon energies were calibrated using the Au $4f_{7/2}$ photoelectron line recorded on a gold disc contained on the sample holder.

The NPs samples were spin-coated on conductive glass (FTO) with a subsequent annealing at 330^{o}C for 30 mins. Fixed analyzer transmission mode was used, in medium area mode, with pass energies of 10 eV for photon energies up to 1040 eV in an additional broadening of the photoelectron peaks due to the electrostatic analyzer contribution by 0.24 eV (at 10 eV pass energy). Scans of the most intense photoelectron peak for the three elements of interest were each recorded at photon energies to give four different photoelectron kinetic energies (KE). The use of the same photo-electron kinetic energy can obtain the sample depth information for all the elements. Those four excitation photon energy allowed us to have similar photo-electron kinetic energy(350 eV、550 eV、750 eV) for three elements. We employed those three photo-electron kinetic energy to understand the depth distribution of Pt、Pd and Ru elements for Pt/Ruc@Pds. The atomic ratio of elements was estimated by the emission peak area normalized by the photon ionization cross section and the photon flux of excitation photon energy for each elements.[1, 2] The results were summarized in below.

2. Crystal symmetry inspection

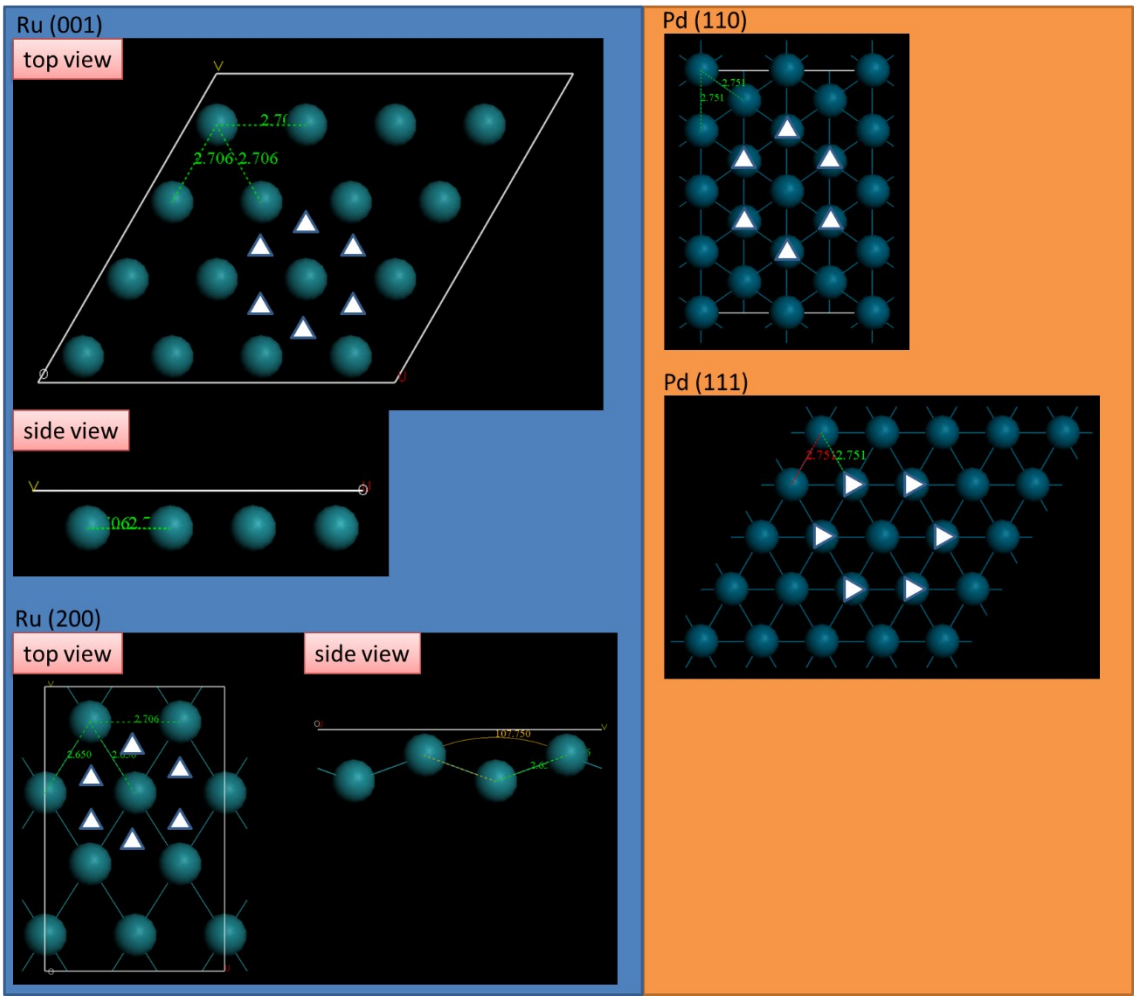

Fig. S2 The lattice slice for Pd (111) (110) and Ru (110) facets.

As denoted by the white triangles, the Pd (110) and (111) facets possess the same symmetry and interatomic distances with that of Ru (001). In this case, the Pd atoms can allocate at the hollow sites of Ru(001) without experiencing lattice strain. Given that Ru(200) facet are twisted to the angle of 107.5° at surface, the Pd (111) and (110) facets will experience a compression lattice strain upon allocating to this place.

3. X-ray photoemission spectroscopy depth profile inspection

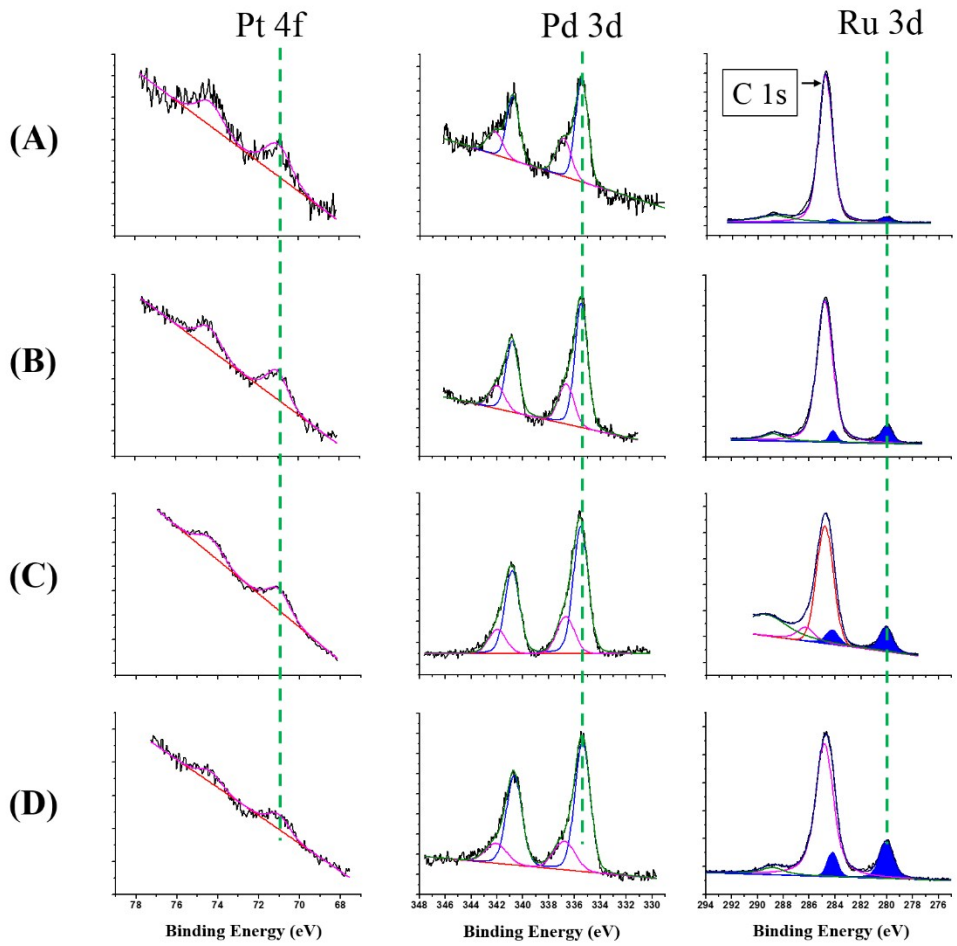

Fig. S3 X-Ray Photoelectron Spectra of Pt 4f、Pd 3d and Ru 3d for $Pt/Ru_c@Pd_s$ NPs. The excitation photon energy is (A) 440 eV, (B) 645 eV, (C) 800 eV, and (D) 1040 eV.

Photo-electron kinetic energy	Detection depth	Atomic ratio of Pt	Atomic ratio of Pd	Atomic ratio of Ru
~ 350 eV	~ 2.4 nm	2.2%	39.1%	58.7%
~ 550 eV	~ 3.6 nm	2.8%	38.7%	58.5%
~ 750 eV	~ 4.2 nm	3.4%	37.9%	58.7%

4. Valence band spectra of reference compared to experiment samples

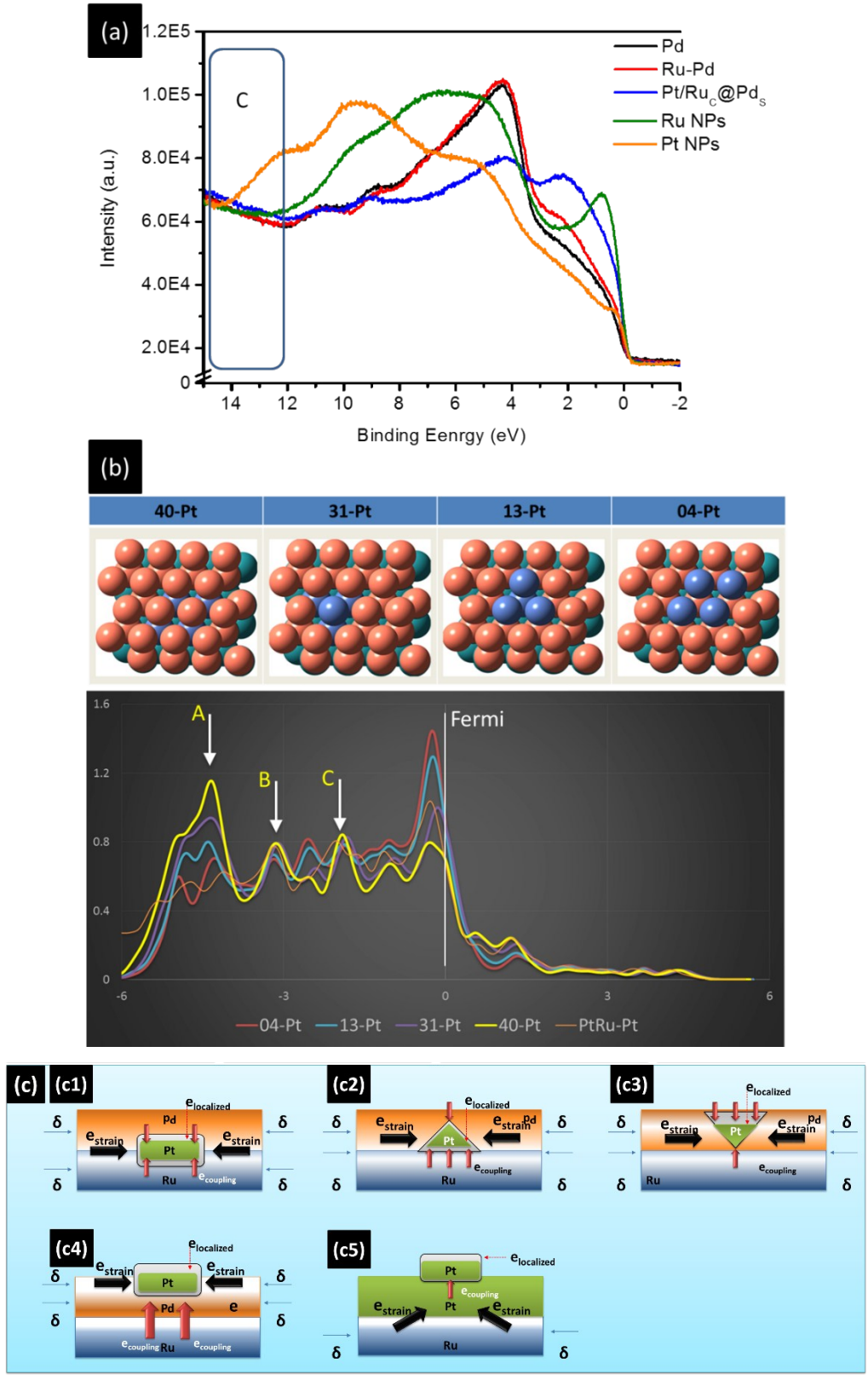

Fig. S4 (a) The VB spectra of Ru and Pt NPs; (b) the DFT calculated DOS of Ru(001)@Pd model with 4-atoms Pt cluster in different configuration; (c) scheme for the heterojunction induced electron relocation in 40-Pt (c1), 31-Pt (c2), 13-Pt (c3), 04-

Pt (c4), and $Pt^{cluster}$-Ru(001)@Pt (c5).

In Fig. S4a, as clearly indicated, the VB spectrum of Ru NPs possesses the highest intensity in the near Fermi-level states among that of all NPs. This character evident its strong reduction activity for I_3^- reduction. However, the Ru atoms tends to donate the valence electron in formation of compound. It thus forming a strong barrier for accepting the electrons from FTO collectors for regenerating it's the reaction sites and thus suppressing the chemisorption of O: radicals. The strong electron donation of Ru is a positive factor for reducing the activation of reaction sites and thus the ORR onset potential.

The DOS of models for Pt cluster in different configurations atop the Ru(001)@Pd slab are compared in Fig. S4b. The models of 40-Pt, 31-Pt, 13-Pt, and 04-Pt denote the structure of 4 Pt atoms at follow sites of the Pd-Ru interface, the 4 Pt atoms stack in tetragonal cluster where 3 atoms at the Ru follow sites, the 4 Pt atoms stack in tetragonal cluster where 1 atom at the Ru follow sites, and the 4 Pt atoms stack at the Pd follow sites at the topmost layer of Pd. It is important to note that the DOS features are strongly dominated by the atomic stacking configuration of the heterojunctions. As indicated, the 40-Pt possesses the lowest DOS intensity in near-Fermi level among the presenting models. A strong DOS in the near-core region is found at -4.6 eV (peak A). These features indicate the strong electron preservation effects due to the coupling effects of Ru-Pt-Pd heterojunction. In this case, the Pt cluster possess a strong electronegative dipole and local compression lattice strain at the Ru-Pd interface (see Scheme S1) that extracting the valence electrons from Ru and Pd region. Such local lattice compression effect and the dipole electron relocation are evidently shown by the significant splitting of DOS peaks (B and C). Consequently, the center of d-band is slightly shifted down by 0.2 – 0.4 eV compared to the presented models. By relocate the Pt atoms into tetragonal cluster with 3 atoms face to the Ru interface (31-Pt), the DOS in near-Fermi level is increased by 0.2 (a.u.) with a suppression of peak D by 0.28 (a.u.) compared to that of 40-Pt. These charge relocations are substantially enhanced by relocating the Pt atoms to the topmost layer (04-Pt) of Pd and again proving the substantial localized lattice strain and electronegative dipole around Pt clusters; where the near-Fermi peak is substantially increased by 0.61 (a.u.) with the suppression of peak A by 0.51 (a.u.). In this case, the Pt cluster form a heterojunction of Pt-Pd-Ru coupling. This coupling effect triggers a strong electronic dipole and thus resulting in the electron relocation to Pt clusters at the outmost layer of the NPs. The DOS of Pt cluster at Ru(001)@Pd model was compared as reference to prove the interface coupling effect. In this model, the Pt cluster was placed atop the hollow sites

of Pt top layer at the Ru(001) substrate. From the obtained DOS feature, one can notice that the intensity of its near-Fermi peak is slightly increased by 0.1 (a.u.) with the splitting of peak D into three states and the suppression of intensity comparing to that of 31-Pt. These features demonstrate that the interface strain effect of Pt clusters in Ru@Pd surface is stronger than they are in the Ru interface (40-Pt and 31-Pt); where indirect coupling between Pt and Ru domain (i.e., 04-Pt and 13-Pt model) injects the electrons to the Pt clusters at the topmost layer of Pd from Ru and Pd regions) via the potential tunnels building via local strain.

5. CO stripping test on $Pt/Ru_C@Pd_S$ NPs

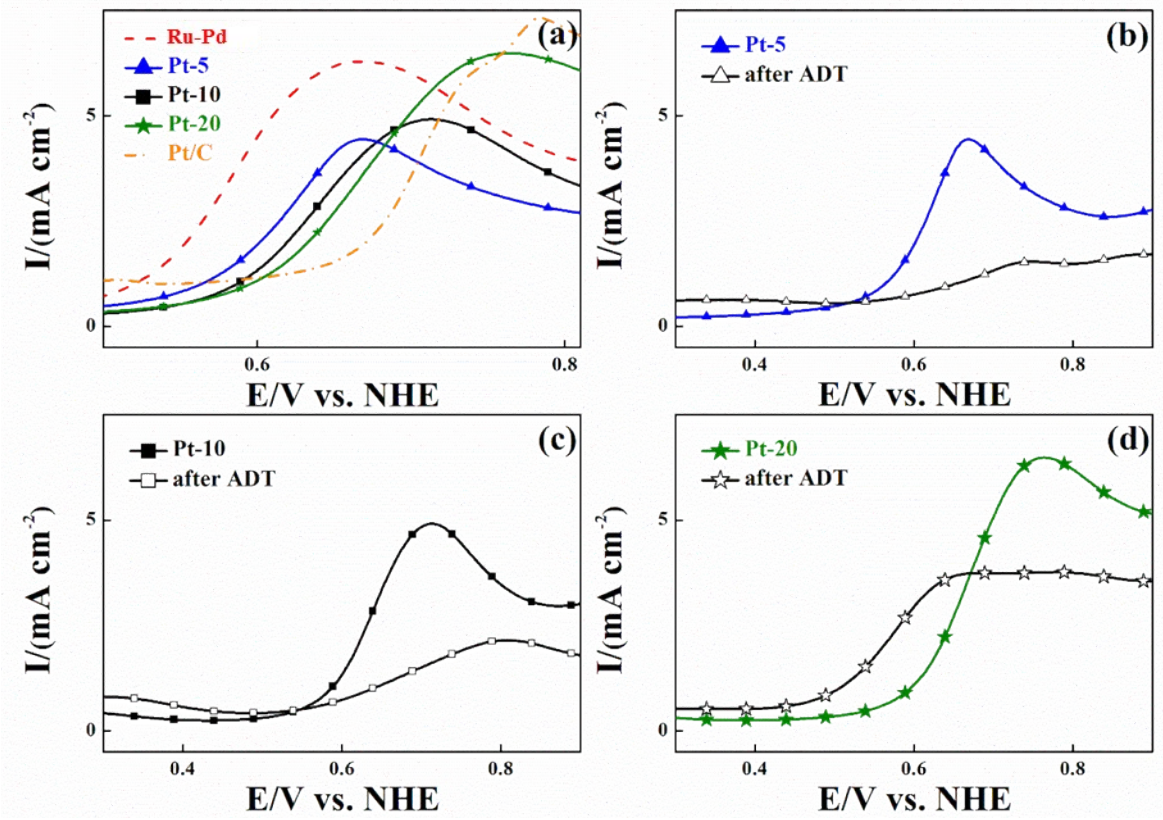

Fig. S5 CO stripping curves of (a) Ru-Pd compares with $Pt/Ru_C@Pd_S$ and carbon supported Pt NPs. (b), (c), (d) the CO stripping curves of $Pt/Ru_C@Pd_S$ NPs containing Pt/Pd = 5, 10, and 20 at%.

6. ORR curves of Pd-Pt NP with Pt/Pd ratios from 0.1 to 0.3 compared with that of CNT supported Pd and Pt NP and commercial carbon supported Pt NP (JM – Pt/C)

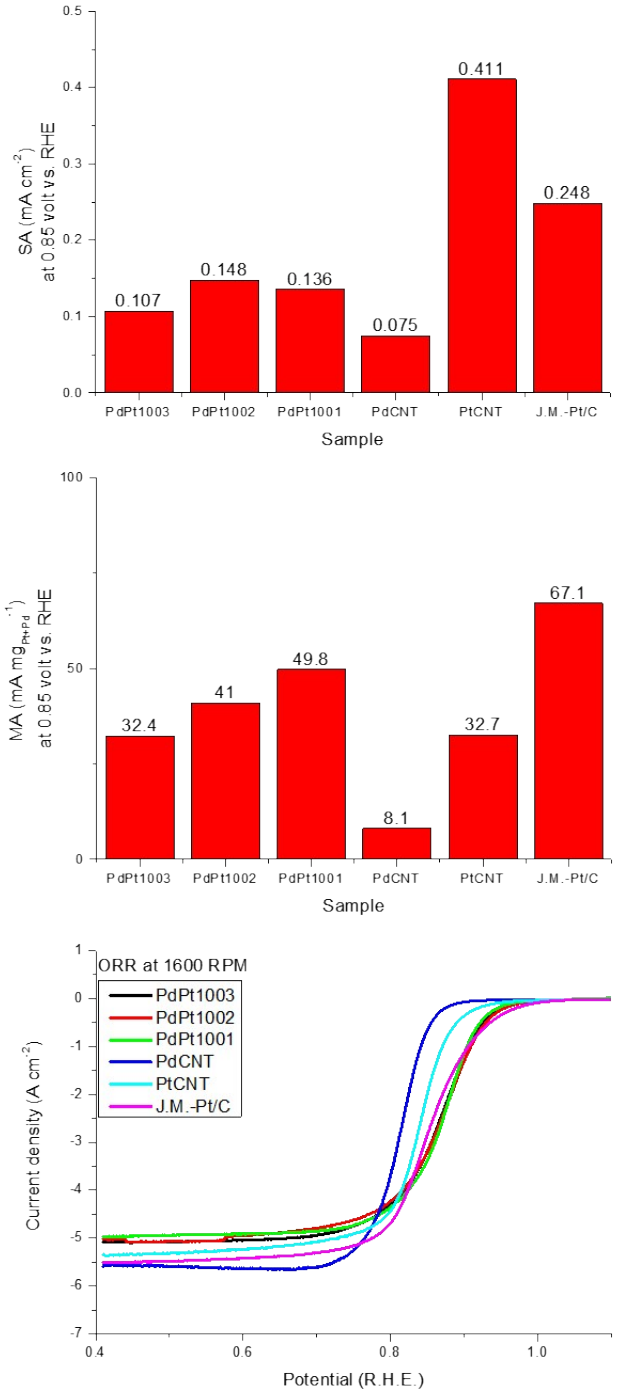

Fig. S6 linear sweep voltammetry (LSV) spectra of CNT supported Pt doped Pd NP, Pd, Pt NPs, and commercial carbon supported Pt NP (JM-Pt/C) for oxygen reduction; PdPt1001, PdPt1002, and PdPt1003 denote NP in PdcorePtshell structure with Pt/Pd ratios of 0.1, 0.2, and 0.3, respectively. Rotation speed of electrode is 1600 rpm.

The mass activity (MA) of the catalysts are obtained by using the following equation:

$$MA = I_{0.85} / [Pt]$$

where $I_{0.85}$ represented the current density at 0.85 volt vs. RHE and [Pt] represented the Pt loading (mg cm^{-2}) in the electrode. The Pt metal loading of Pt-5, Pt-10, Pt-20, and Pt/C in the catalysts is 0.5, 1, 2, and 40 wt%, respectively based on the inductively coupled plasma-atomic emission spectroscopy (ICP-AES, Jarrel-Ash, ICAP 9000) results.

Fig. 6S compares the LSV curves of experimental NP compared with that of control samples (CNT supported Pd, Pt NPs and commercial carbon supported Pt NP (JM-Pt/C)); where corresponding specific surface activity (SA) and mass activity (MA) are given in above. Obtained parameters are summarized in Table S3. As elucidated, PdPt1002 gain the highest onset potential (E_{onset}) of 0.927 volt vs. RHE among these samples. This value is 0.03 volt lower indicating its higher threshold energy for oxygen reduction than that of Pt-20 ($Pt/Ru_C@Pd_S$ NP with Pt/Pd = 0.2). This statement is further confirmed by the charge transfer number of 3.3 to 3.5, therefore, indicating the multi-pathways of oxygen reduction in PdPt1001 – 1003 NPs surface. In addition, MA of PdPt NPs is increased from 91.3 to 321.3 mA $mgPt^{-1}$ at 0.85 volt with Pt from 0.3 to 0.1. This parameter is substantially improved by ~1347 (~1380%) and 1310 (~420%) mA $mgPt^{-1}$ by intercalating Pt cluster to $Ru_C@Pd_S$ NP with the same Pt/Pd ratios, therefore, features the substantially activated Pt clusters in oxygen reduction reaction atop $Pt/Ru_C@Pd_S$ NP.

Table S3 Electrochemical parameters of experimental NPs in ORR reaction test

Sample	E_{onset} (volt vs. RHE)	n	J_K (mA cm^{-2})	MA		
				mA mg_{Pt}^{-1}	mA mg_{Pd}^{-1}	mA mg_{Pd+Pt}^{-1}
PdPt1003	0.927	3.5	8.19	91.3	50.2	32.4
PdPt1002	0.931	3.3	9.49	152.8	56.0	41.0
PdPt1001	0.920	3.5	10.38	321.3	58.9	49.8
Pt-20	0.954	3.8	11.54	698.0	380.0	317.0
PdCNT	0.854	3.8	0.74		8.1	8.1
PtCNT	0.882	3.9	3.00	32.7		32.7
JM-Pt/C	0.913	4.0	5.34	67.1		67.1

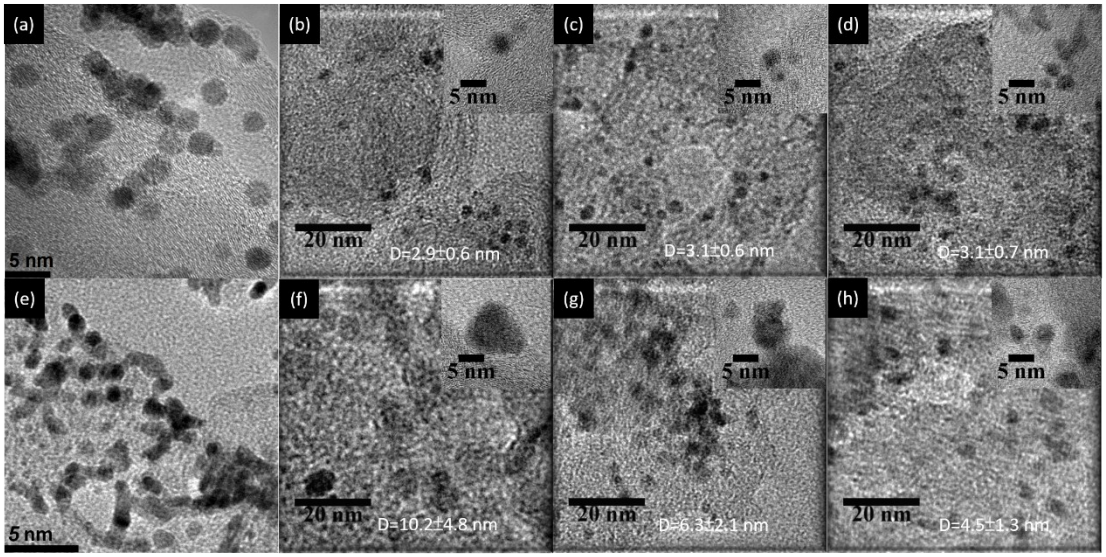

Fig. S7 TEM images of pristine JM Pt/C (a), Pt-5 (b), Pt-10 (c), and Pt-20 (d) NPs. The images of the Pt/C and three NPs after ADT are shown in (e), (f), (g), and (h).

Results of EDS map for Ru-Pd (the control sample) and Pt/Ru@Pd (Pt-10, the case of optimum ORR MA) NPs are given Fig. S8. These images were observed by using TEM-FEI Osiris platform with four detector EDS system (Oxford) at out sourcing vendor (MSSCORP CO., LTD). Given that the presented results are conducted by TEM with the best resolution we can access, only results of NP with best ORR activity (Pt-20) and control sample are conducted as representative information in our study. As indicated, it presents the significant index to the restructure of Pd cluster into PdPt shell structure. Shown in Fig. S8a, Pt atoms are mostly distributed in local region (upper of left hand side, where shows the high density of Pd atoms) in Pt/Ru@Pd NC. This phenomenon consistently explains the preferential formation of

Pt cluster in Pd region with the restructure of Ru-Pt into Pt/Ru@Pd NP. However, the weak signal to noise ratio hinders the further high resolution analysis. This is caused by the small scattering matter of such a 5-8 nm single particle. For Ru-Pd (Fig. S8b), the anisotropic EDX map consistently explains the formation of cluster-in-cluster Ru-Pd NC; where Ru is riched in particle core and Pd is riched in particle edge (denoted by yellow arrows). Such a distribution again rationalizes the restructure of Ru-Pd into Pt/Ru@Pd NP (consisting of PdPt alloy shell or cluster at Pd shell structure).

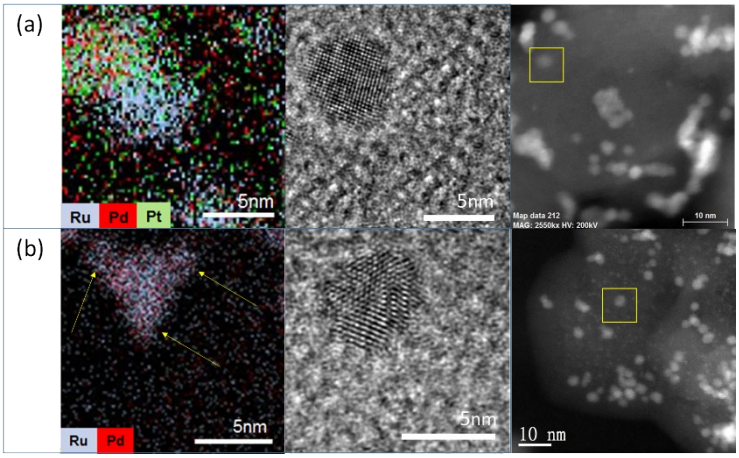

Fig. S8 EDX map, bright field HRTEM, and HADFF images (from left to right) of (a) Pt-20 (Pt/Ru@Pd) and (b) Ru-Pd NPs.

References

[1] S. Ghosal, J. C. Hemminger, H. Bluhm, B. S. Mun, E. L. D. Hebenstreit, G. Ketteler, D. F. Ogletree, F. G. Requejo, M. Salmeron *Science*. **2005**, 307, 563-566.

[2] N. J. Divins, I. Angurell, C. Escudero, V. Pérez-Dieste, J. Llorca *Science*. **2014**, 346, 620-623.

[3] Y. Sun, Y. Xia *Advanced Materials*. **2002**, 14, 833-837.

[4] J.-M. Lin, T.-L. Lin, U.-S. Jeng, Y.-J. Zhong, C.-T. Yeh, T.-Y. Chen *Journal of Applied Crystallography*. **2007**, 40, s540-s543.